IEEE Access
Multidisciplinary | Rapid Review | Open Access Journal

Received November 2, 2020, accepted November 4, 2020, date of publication November 10, 2020,
date of current version November 23, 2020.

Digital Object Identifier 10.1109/ACCESS.2020.3037201

Accurate Analysis of Harmonic Transmission of Line Commutated Converter Considering Firing Angle Fluctuation

HE HUANG, JUNPENG MA, (Member, IEEE), SHUNLIANG WANG, (Member, IEEE), YUQING DONG, NING JIAO, (Student Member, IEEE), AND TIANQI LIU, (Senior Member, IEEE)
College of Electrical Engineering, Sichuan University, Chengdu 610065, China
Corresponding author: Junpeng Ma (junpeng_ma@163.com)

This work was supported by the National Natural Science Foundation of China (No. 51977135).

ABSTRACT Line commutated converter (LCC) has been widely applied in hybrid high voltage direct current (HVDC) transmission system, where the modular multilevel converter (MMC) is applied as receiving end and may induce low order harmonics in DC-link voltage. These low order harmonics will introduce the low frequency fluctuation into the control loop of LCC and complex the harmonics analysis. The traditional method to calculate LCC harmonics is derived by the switching function and modulation theory, which only obtains characteristic harmonics. The low-frequency fluctuation superimposed on the firing angle in the control system is ignored in the traditional method. In this paper, the interharmonics, which is introduced by firing angle fluctuation, is revealed by the double Fourier method. A fitting function method is applied for depicting the varied commutation overlap caused by firing angle fluctuation. Compared to the traditional method, the proposed method can effectively analyze both characteristic harmonics and interharmonics in the condition of low-frequency fluctuation of the firing angle. The accuracy and effectiveness of the theoretical analysis are verified with a three-phase LCC rectifier built in PSCAD/EMTDC and experimental test.

INDEX TERMS Hybrid HVDC, interharmonics, firing angle fluctuation, overlap angle fluctuation, harmonic analysis.

I. INTRODUCTION

The hybrid high voltage direct current (HVDC) system adopts line commutated converter (LCC) at rectifier side and modular multilevel converter (MMC) at inverter side. This hybrid topology reduces the manufacture and operating cost, eliminates the commutation failure which is inevitable in LCC-based inverter [1], [2]. However, some control strategies of MMC will cause resonance in DC-side [3]–[6], whose low frequency fluctuations will be introduced in the LCC rectifier control loop. Consequently, the firing angle calculated by the control loop contains ripples and causes DC-side voltage harmonic pollution, even system oscillation [7], [8]. Therefore, it is of great significance to perform a quantitative analysis of the harmonics for hybrid HVDC system with firing angle fluctuations.

The associate editor coordinating the review of this manuscript and approving it for publication was Enamul Haque.

The operation of the LCC-HVDC converter is naturally defined by time-domain differential and algebraic equations. This suggests time-domain simulation and Fourier analysis as a possible method. The switching function and modulation theory can be applied to explain the transmission mechanism of characteristic harmonics [9]. Furthermore, a precise mathematical model has been developed by the unbalanced switching functions, which can be used for harmonics analysis in the condition of the unbalanced power supply and unbalanced system impedance [10]–[12]. As demonstrated in [13], the space vector is first used for harmonic analysis to illustrate the frequency transformation mechanism of converters. It is also valid for both voltage-source and current-source converters with asymmetrical modulation. However, the long simulation time is required to reach a steady-state in these methods. To assure efficiency and accuracy in time-domain simulation, the exact switching function is obtained in [14] by iteratively solving the switching instants. Yet, the approach relies on sampled data and iterative

initial values. None of these methods takes interharmonics into account.

The switching of current conduction from one phase to another is referred to as the commutation process, which cannot be neglected in harmonic analysis. The commutation process is only modeled as a proportional coefficient in switching function [9], yet the derivation process is not addressed. The generation mechanism of characteristic harmonics considering the commutation is explained concretely in [15]. Meanwhile, [16] gives a DC-side equivalent circuit during the commutation process by paralleling commutation branches. Better modeling accuracy is achieved by this method compared to traditional modulation function approaches. However, the varied overlap angle is not considered by methods mentioned-above.

On the other hand, as an alternative to the traditional approach, harmonic state space (HSS) has attracted scholars' interest in recent years. This method is based on the linear time-periodic (LTP) theory, which has been widely applied to analyze the harmonic coupling and stability in a large power network [17]–[19]. Nevertheless, HSS is too complex to calculate harmonics since high order state-space matrix needs to be established. Meanwhile, HSS can only deal with the characteristic and uncharacteristic harmonic coupling, yet the interharmonics are not considered.

It is well known that there are abundant filters applied in practical HVDC projects to improve power quality [20]–[22]. Any filter, however, has its fixed cut-off frequency which cannot cover all frequency range. Therefore, the DC-side low-frequency current fluctuations, which comes from inverter based MMC and cannot be completely filtered, are introduced into the proportional-integral (PI) regulator for DC-side current control of LCC. The output firing angle of the PI regulator thereby has a low-frequency ripple, and then this firing angle with ripple is compared with phase angles to generate the individual driving pulses for each thyristor with varied intervals. The commutation overlap angle also fluctuates due to this low-frequency ripple. The variation of firing interval means unequal conduction time of each thyristor and introduces interharmonics.

Interharmonics are spectral components at frequencies that are not integer multiples of the system fundamental frequency (50Hz in general). Some of the most remarkable issues related to interharmonic theory are presented in [23], including detailed definitions and concepts. The letter [24] proposed a method to determine the existence of interharmonics in the discrete Fourier transform (DFT) results. The interharmonic generation process in motor drive applications is investigated in [25], and the effects of modulation techniques are also taken into account [26]. However, the mechanism of interharmonic transmission in LCC has not been addressed in previous researches.

The motivation of this paper is to distinctly illustrate the mechanism of interharmonic transmission derived from firing angle fluctuation and subsequent commutation overlap angle vibration. The main contributions of this paper could be summarized as follows:

1) Based on the individual phase control of firing angle in the converter, the turn-on and turn-off instant of each thyristor can be described exactly, and the mechanism of interharmonic transmission derived from a variation of firing interval in LCC is first illustrated.
2) In the analysis for harmonic transmission of LCC, the effect of dynamic commutation overlap angle is first included by the Fourier series fitting.
3) The proposed method for the accurate harmonic analysis can not only calculate characteristic harmonics but precisely analyze interharmonics. Especially, the interharmonics are not considered in the previous method.

The rest of the paper is organized as follows. In section II, the harmonic transmission is derived from firing pulse generation principle in a single thyristor without the commutation overlap, and the interharmonic calculation progress is also given in detail with the double Fourier series analysis. Furthermore, based on the Fourier series fitting, the dynamic commutation overlap angle is considered in section III. The interharmonic calculation in a rectifier is presented in section IV. Then, the simulation in PSCAD/EMTDC and the experimental test is carried out to validate the proposed approach in section V and section VI. Simulation results and experimental test validate the accuracy of the proposed method. Finally, the conclusions are summarized in section VII.

II. HARMONIC TRANSMISSION ANALYSIS IN A THYRISTOR WITHOUT COMMUTATION OVERLAP

In this section, the interharmonic generation and transmission characteristics for the single thyristor are investigated without commutation overlap, which makes the foundation for subsequent sections.

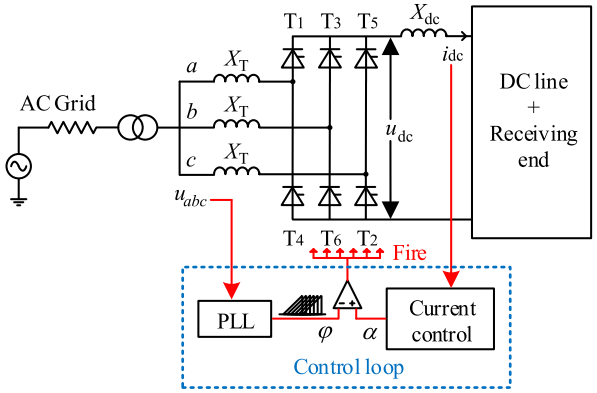

FIGURE 1. Three-phase rectifier bridge.

The three-phase rectifier bridge consists of six thyristors that are numbered according to the conduction sequence (see Fig.1). The turn-off instant of a thyristor depends on the turn-on instant of the next thyristor in the same upper or lower

bridge arm. Take thyristor T_1 for instance, it is turned off as soon as T_3 is turned on.

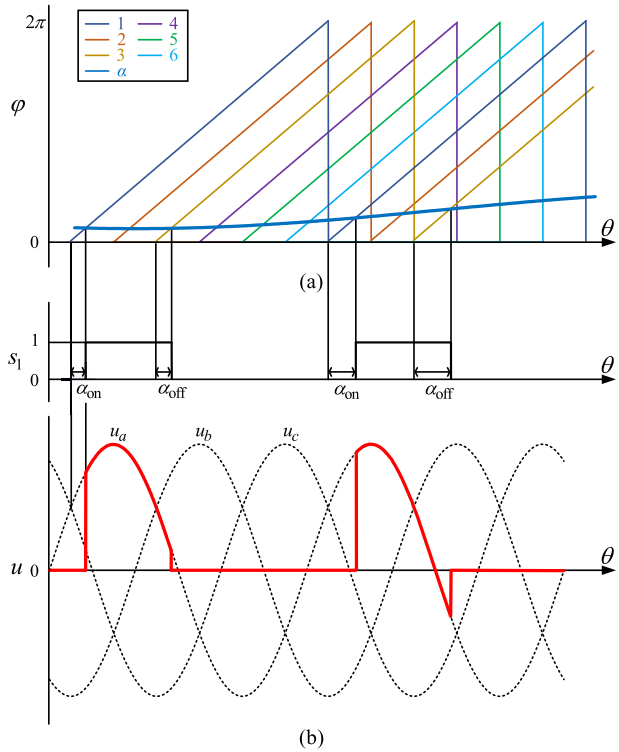

FIGURE 2. Firing pulse generation principle. (a) Firing pulse generation. (b) Thyristor states and corresponding DC voltage.

The generation principle of the firing pulse is shown in Fig. 2(a). The firing angle signal is compared with the phase angle of each phase voltage calculated by the phase-locked loop (PLL) to generate the driving pulses, which also indicate the switching state of the thyristor. The firing angle also determines the phase voltage which is output in DC-side shown in Fig. 2(b).

All periodic ripples could be rewritten as Fourier series. So it is assumed that there is a sinusoidal fluctuation with very low frequency in firing angle signal. Hence, the thyristor operation state can be modeled as a periodic function that can be expressed as $s_1(x, y)$ in a period of variable y by (1).

$$s_1(x,y) = \begin{cases} 1, & x_{on} \le x \le x_{off} \\ 0, & -\pi \le x < x_{on} \text{ or } x_{off} < x \le \pi \end{cases} \tag{1}$$

where x is phase angle from PLL and y is the phase angle of sinusoidal fluctuation in firing angle, they can be described in detail by (2).

$$\begin{cases} x = \omega_x t + \theta_x \\ y = \omega_y t + \theta_y \end{cases} \tag{2}$$

where ω_j and θ_j are the frequency and initial phase of signal j ($j = x, y$), respectively. Thus, the firing angle can be described by (3).

$$\alpha = \alpha_0 + M \cos y \tag{3}$$

where α_0 is the command value of firing angle, M is the amplitude of sinusoidal fluctuation in firing angle. The phase angle from PLL to thyristors T_1 and T_3 can be represented by β_1, β_3 respectively in (4).

$$\begin{cases} \beta_1 = x - 2k\pi \\ \beta_3 = x - 2k\pi - \dfrac{2\pi}{3} \end{cases} \tag{4}$$

The phase angles of T_1 at turn-on instant (x_{on}) and turn-off instant (x_{off}) in one fundamental period are shown in (5), which can be inferred from (3), (4) and Fig. 2(b).

$$\begin{cases} x_{on} = \alpha_{on} = \alpha_0 + M \cos y \\ x_{off} = \alpha_{off} = \alpha_0 + M \cos y + \dfrac{2\pi}{3} \end{cases} \tag{5}$$

where α_{on} and α_{off} are firing angles at turn-on instant and turn-off instant, respectively.

Substituting (5) to (1), and double Fourier series analysis is applied to calculate interharmonics caused by a single thyristor shown in (6).

$$\begin{aligned} s_1(x,y) = \frac{1}{3} &+ \sum_{m=1}^{\infty} (A_{m0} \cos mx + B_{m0} \sin mx) \\ &+ \sum_{m=1}^{\infty} \sum_{\substack{n=-\infty \\ n\neq 0}}^{\infty} [A_{mn} \cos (mx + ny) \\ &+ B_{mn} \sin (mx + ny)] \end{aligned} \tag{6}$$

Equation (6) is the basis of the accurate analysis for the harmonic transmission of LCC with firing angle disturbance. There are three items in (6): the first is DC component, the second is fundamental ($m = 1$) and harmonic component of the sawtooth carrier (the output of PLL), and the last is sideband harmonic component, which is distributed on both sides of carrier harmonics with integral multiple frequency intervals (ω_y). And the coefficients are illustrated in (7).

$$\begin{cases} A_{m0} = \dfrac{2}{\pi m} \sin \dfrac{m\pi}{3} J_0(mM) \cos m(\alpha_0 + \dfrac{\pi}{3}) \\ B_{m0} = \dfrac{2}{\pi m} \sin \dfrac{m\pi}{3} J_0(mM) \sin m(\alpha_0 + \dfrac{\pi}{3}) \\ A_{mn} = \dfrac{2}{\pi m} \sin \dfrac{m\pi}{3} J_n(mM) \cos(\dfrac{n\pi}{2} + m(\alpha_0 + \dfrac{\pi}{3})) \\ B_{mn} = \dfrac{2}{\pi m} \sin \dfrac{m\pi}{3} J_n(mM) \sin(\dfrac{n\pi}{2} + m(\alpha_0 + \dfrac{\pi}{3})) \end{cases} \tag{7}$$

where J_n is the Bessel function with order n. The influence of the firing angle ripple on the harmonic amplitude is considered by the Bessel function.

III. HARMONIC ANALYSIS OF A THYRISTOR WITH COMMUTATION OVERLAP

The leakage inductance of the converter transformer will lead to an overlap angle. Based on section II, this section elaborates the interharmonic generation and transmission caused by a single thyristor with the overlap angle in the condition of firing angle fluctuation.

A. THE STATE FUNCTION $S_1(x, y)$ OF THYRISTOR CONSIDERING COMMUTATION OVERLAP

Generally, DC-side current maintains constant in the LCC rectifier. In this case, the overlap angle could be calculated in [27] by (8).

$$\mu = \cos^{-1}(\cos\alpha - \frac{2X_{\mathrm{T}}I_{\mathrm{dc}}}{\sqrt{3}U_{\mathrm{p}}}) - \alpha \tag{8}$$

where μ is the overlap angle, I_{dc} is the equilibrium value of DC-side current, U_{p} is the amplitude of AC phase voltage, X_{T} is equivalent leakage inductance of converter transformer (see Fig.1), and it can be described as (9).

$$X_{\mathrm{T}} = \frac{V_S\%}{100}\frac{V_N^2}{S_N} \tag{9}$$

where $V_S\%$, V_N and S_N are the short-circuit voltage, rated line voltage and the rated capacity of converter transformer, respectively.

Equation (8) depicts the nonlinear relationship between α and μ, which are trigonometric and anti-trigonometric functions. However, these functions cannot change the frequency of the fundamental signal. Thus, as shown in Fig. 3, when there is a sinusoidal disturbance in the firing angle α, the overlap angle μ will fluctuate at the same frequency and is negatively correlated with α. That is, the larger α, the smaller μ.

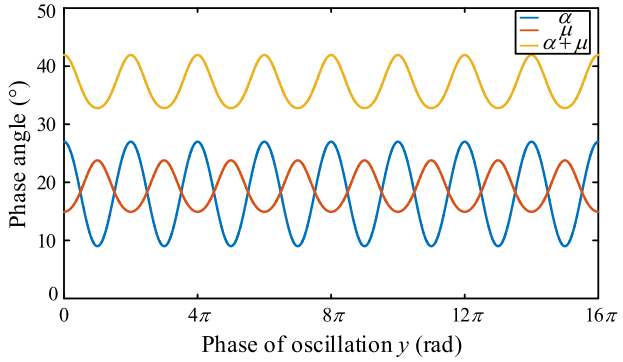

FIGURE 3. The changing curves of overlap angle μ with the disturbed firing angle α.

Considering commutation overlap angle disturbance caused by firing angle fluctuation, the conduction state of thyristor and the corresponding AC voltage is shown in Fig. 4. The overlap angle μ is not a constant value, but a function of firing angle α. Namely, the length of the commutation is determined by the firing angle. Similar to (1), taking overlap angle fluctuation into account, the thyristor operation state can be expressed as (10), where 1/2 means that half of the phase voltage contributes to DC-side voltage during commutation overlap duration.

$$S_1(x,y) = \begin{cases} 1, & x_{\mathrm{on}} + \mu_{\mathrm{on}} \le x \le x_{\mathrm{off}} \\ \frac{1}{2}, & x_{\mathrm{on}} < x_{\mathrm{on}} + \mu_{\mathrm{on}} \text{ or } x_{\mathrm{off}} < x \le x_{\mathrm{off}} + \mu_{\mathrm{off}} \\ 0, & -\pi \le x < x_{\mathrm{on}} \text{ or } x_{\mathrm{off}} + \mu_{\mathrm{off}} < x \le \pi \end{cases} \tag{10}$$

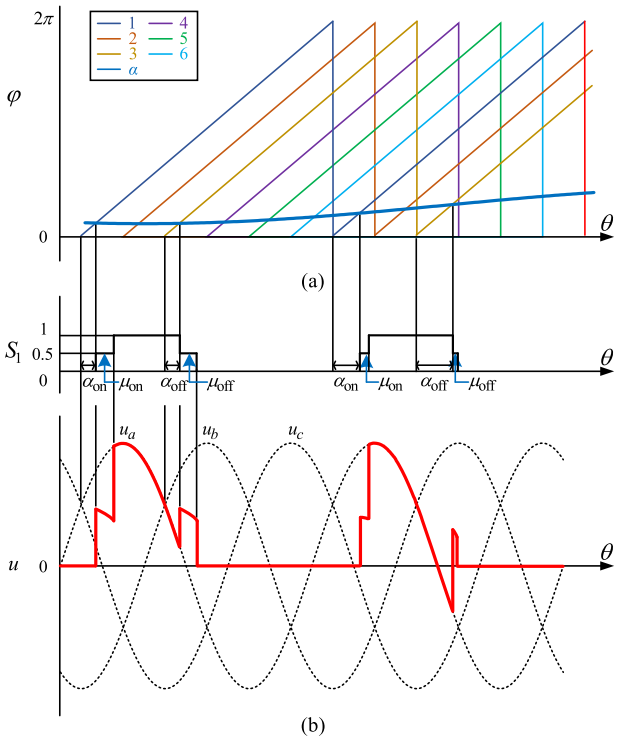

FIGURE 4. Firing pulse generation principle with commutation. (a) Firing pulse generation. (b) Thyristor states and corresponding DC voltage.

where μ_{on} and μ_{off} are overlap angles at turn-on instant and turn-off instant respectively, which can be derived from (8).

$$\begin{cases} \mu_{\mathrm{on}} = \cos^{-1}[\cos\alpha_{\mathrm{on}} - 2X_{\mathrm{T}}I_{\mathrm{dc}}/\sqrt{3}\,U_{\mathrm{p}}] - \alpha_{\mathrm{on}} \\ \mu_{\mathrm{off}} = \cos^{-1}[\cos\alpha_{\mathrm{off}} - 2X_{\mathrm{T}}I_{\mathrm{dc}}/\sqrt{3}\,U_{\mathrm{p}}] - \alpha_{\mathrm{off}} \end{cases} \tag{11}$$

B. FITTING TRIGONOMETRIC FUNCTION $\alpha + \mu$

By comparing equation (1) with (10), it can be seen that the thyristor operation state includes on-state, off-state, and commutation state. When the thyristor is turned on or off, the commutation ending angle could be obtained as (12) by combining (3), (5) and (11).

$$\begin{cases} x_{\mathrm{on}} + \mu_{\mathrm{on}} = \alpha_{\mathrm{on}} + \mu_{\mathrm{on}} = \cos^{-1}(\cos\alpha_{\mathrm{on}} - \dfrac{2X_{\mathrm{T}}I_{\mathrm{dc}}}{\sqrt{3}\,U_{\mathrm{p}}}) \\ x_{\mathrm{off}} + \mu_{\mathrm{off}} = \alpha_{\mathrm{off}} + \dfrac{2\pi}{3} + \mu_{\mathrm{off}} \\ \qquad = \cos^{-1}(\cos\alpha_{\mathrm{off}} - \dfrac{2X_{\mathrm{T}}I_{\mathrm{dc}}}{\sqrt{3}\,U_{\mathrm{p}}}) + \dfrac{2\pi}{3} \end{cases} \tag{12}$$

Applying the double Fourier method to (10) directly, the harmonic distortion cannot be derived due to inverse trigonometric function in (12) and limitation of Bessel function. On the foundations of integral requirements and similar trigonometric properties (see Fig.3), the function $\alpha + \mu$ could be rewritten as Fourier series. A fitting result is obtained by retaining the DC component and fundamental components in the Fourier series. The fitting result has the same form as α

expressed in (13).

$$\alpha + \mu = a_0 + a_1 \cos y \tag{13}$$

where a_0 and a_1 are Fourier coefficients, which could be calculated by (14),

$$\begin{cases} a_0 = \dfrac{\omega_y}{2\pi} \displaystyle\int_0^{\frac{2\pi}{\omega_y}} (\alpha + \mu) dt \\ a_1 = \dfrac{\omega_y}{\pi} \displaystyle\int_0^{\frac{2\pi}{\omega_y}} (\alpha + \mu) \cos \omega_y t dt \end{cases} \tag{14}$$

Substituting (12), (13) and (14) into (10), interharmonics could be calculated in (15).

$$\begin{aligned} S_1(x, y) = \frac{1}{3} &+ \sum_{m=1}^{\infty} (A'_{m0} \cos mx + B'_{m0} \sin mx) \\ &+ \sum_{m=1}^{\infty} \sum_{\substack{n=-\infty \\ n\neq 0}}^{\infty} [A'_{mn} \cos(mx + ny) \\ &+ B'_{mn} \sin(mx + ny)] \end{aligned} \tag{15}$$

Equation (15) is consistent with (6) in structure and physical meaning, and the coefficients are illustrated in the Appendix. Compared to (7), the coefficients of (15) expressed by (A.1) have two similar items: the first has the same structure and physical meaning with (7), and the other presents the influence of varied commutation overlap angle on the harmonic amplitude. Equation (15) thereby considers the harmonics caused by the firing angle disturbance and the variable overlap angle. As a result, the proposed method is closer to practical operating conditions.

IV. ACCURATE HARMONIC ANALYSIS OF A RECTIFIER

In this section, the switching function is established for a rectifier, where both the firing angle and the overlap angle fluctuate, the double Fourier decomposition results of DC voltage are derived.

As shown in Fig.1, six thyristors are respectively conducting within 120° when the rectifier is under normal conditions. Yet, if the firing command contains ripples, the driving pulse generation instant changes, and the conduction duration of six thyristors is not equal.

For the i-th thyristor, its corresponding firing pulse is still generated by the same output phase angle of PLL. Hence, the conduction state of thyristor i is expressed as (16),

$$S_i(x, y) = S_1\left(x - \frac{(i-1)\pi}{3}, y\right) \tag{16}$$

According to Fig. 1, the switching function of phase a is derived from reverse superposition between $S_1(x, y)$ and $S_4(x, y)$, which is expressed as (17).

$$S_a(x, y) = S_1(x, y) - S_4(x, y) \tag{17}$$

The switching function of phase a can be obtained by substituting (15), (16) into (17). Similarly, the switching function of phase b and c can be also obtained in (18).

$$\begin{aligned} &S_j(x, y) \\ &= \sum_{m=1}^{\infty} C_{m0} J_0(mM) \cos m(x - \alpha_0 - \theta_j) \\ &\quad + \sum_{m=1}^{\infty} C_{m0} J_0(ma_1) \cos m(x - a_0 - \theta_j) \\ &\quad + s \sum_{m=1}^{\infty} \sum_{\substack{n=-\infty \\ n\neq 0}}^{\infty} C_{mn} J_n(mM) \cos[m(x - \alpha_0 - \theta_j) + n(y - \frac{\pi}{2})] \\ &\quad + \sum_{m=1}^{\infty} \sum_{\substack{n=-\infty \\ n\neq 0}}^{\infty} C_{mn} J_n(ma_1) \cos[m(x - a_0 - \theta_j) + n(y - \frac{\pi}{2})] \end{aligned} \tag{18}$$

where S_j and θ_j are the switching functions and the initial phases of phase j ($j = a, b, c$), respectively. The coefficients C_{mn} are illustrated in (19).

$$C_{mn} = \frac{2}{m\pi} \sin \frac{m\pi}{2} \cos \frac{m\pi}{6} \tag{19}$$

a-phase voltage is regarded as a reference, and the three-phase voltages can be expressed specifically by (20).

$$\begin{cases} u_a = U_{\mathrm{p}} \cos x \\ u_b = U_{\mathrm{p}} \cos(x - \dfrac{2\pi}{3}) \\ u_c = U_{\mathrm{p}} \cos(x + \dfrac{2\pi}{3}) \end{cases} \tag{20}$$

where U_{p} is the amplitude of AC phase voltage.

According to modulation theory, the relation between AC and DC voltage in rectifier can be described as

$$u_{\mathrm{dc}} = S_a u_a + S_b u_b + S_c u_c \tag{21}$$

where u_{dc} is the DC voltage output from the rectifier.

Substituting (18), (20) into (21), the harmonic analysis results of DC voltage can be obtained in (22),

$$u_{\mathrm{dc}} = u_{\mathrm{dc1}} + u_{\mathrm{dc2}} \tag{22}$$

where u_{dc1} contains the DC component and the characteristic harmonics with the orders of $6k$ ($k = 1, 2, 3 \ldots$), and u_{dc2} is the sideband harmonic component, which is distributed symmetrically on both sides of corresponding DC component and the characteristic harmonics. The detailed expressions are listed in the Appendix.

V. SIMULATION RESULTS

To verify the interharmonic calculation method proposed in this paper, a three-phase rectifier bridge shown in Fig.1 and the firing pulse generation module are established in PSCAD/EMTDC. Specific parameters are shown in Table 1.

The simulation results are presented in Fig. 5. Fig. 5(a) shows the firing pulse generation principle, where there are six sawtooth signals from PLL and firing angle signal. The DC voltage output of the rectifier is shown in Fig. 5(b),

TABLE 1. Simulation parameters.

Module	Parameter	Value
AC voltage	Amplitude of phase voltage U_p	$220\sqrt{2}$ kV
	Frequency ω_x	50Hz
	Reference phase θ_x	0°
Firing angle	Command value α_0	18°
	Fluctuation amplitude M	9°
	Fluctuation frequency ω_y	10Hz
	Initial phase θ_y	0°
Transformer	Short-circuit voltage V_S%	18
	Rated line voltage V_N	$220\sqrt{3}$ kV
	Rated capacity S_N	1320MVA

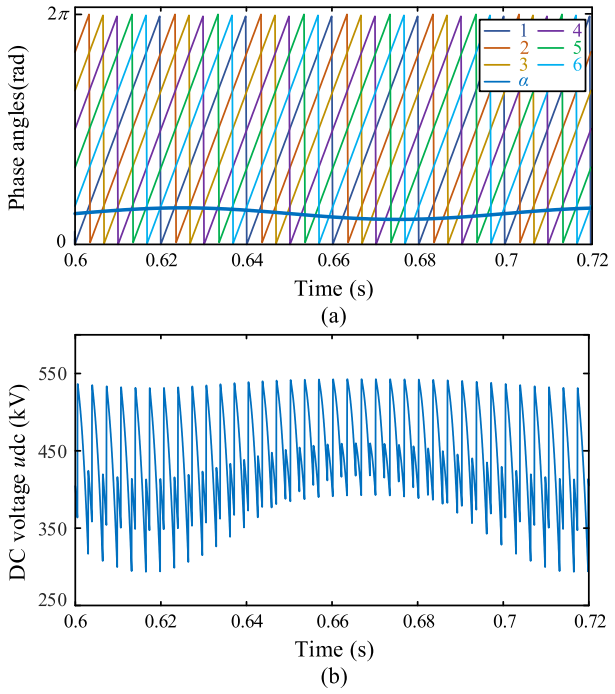

FIGURE 5. Simulation measurements. (a) Firing angle generation principle. (b) DC voltage waveform.

which indicates distinctly that fluctuation superposed on firing angle and subsequent overlap angle is transmitted to the DC voltage.

For the accurate computation of harmonics, function $\alpha + \mu$ should be first fitted according to (14). Fitting results are expressed in (23), and the comparison results are presented in Fig. 6.

$$\alpha + \mu = 36.92 + 4.596 \cos y \tag{23}$$

As shown in Fig. 6, the max fitting error appears at the peak of a trigonometric function, and is not more than 0.5°, which is acceptable.

The spectrum is presented in Fig. 7 to quantitatively analyze the harmonics in DC voltage, where the resolution ratio

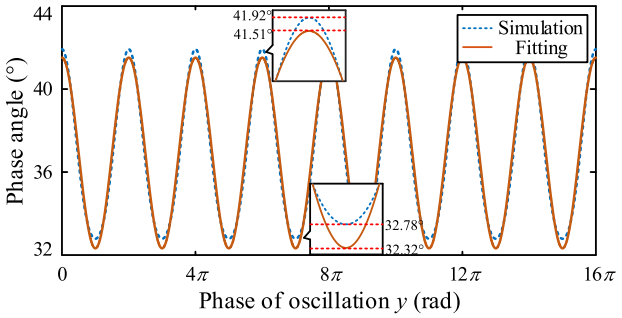

FIGURE 6. Comparison of simulation and fitting results.

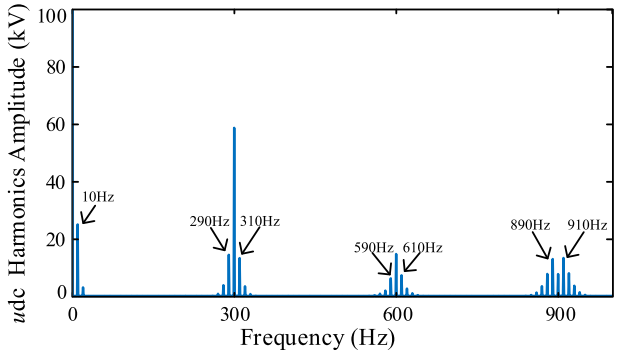

FIGURE 7. DC voltage spectrum.

is 1Hz. The analysis shows that fluctuation superposed on the firing angle signal introduces interharmonics into the system. It can be seen in Fig. 7, these interharmonics are symmetrically distributed on both sides of the original characteristic harmonics with the interval of 10Hz (fluctuation frequency). Especially, when the characteristic harmonics exceed 600Hz, the amplitude of interharmonics on both sides are even larger than that of characteristic harmonics. Yet, these interharmonics are neglected in the traditional analyzing method.

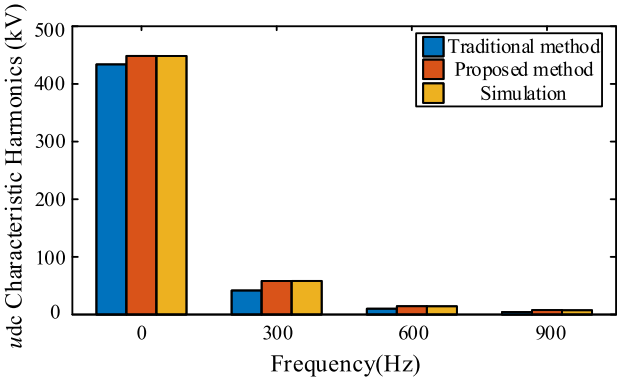

FIGURE 8. Characteristic harmonics comparison between the previous and the proposed methods.

Additionally, the proposed method is utilized for the harmonic calculation of DC voltage. The characteristic harmonic comparison between the traditional method in [9] and this paper is shown in Fig. 8. The results indicate that

TABLE 2. DC voltage harmonic comparison between previous and proposed method.

Frequency (Hz)	Simulation (kV)	Proposed method(kV)	Error (%)	Traditional method(kV)	Error (%)
0	448.5214	448.5853	0.0142	433.8771	3.265
10	24.9574	24.84	0.4704	-	-
290	14.1875	13.7855	2.8335	-	-
300	58.3335	58.2725	0.1046	41.7573	28.416
310	13.5735	13.7855	1.5619	-	-
590	6.0313	6.1769	2.4141	-	-
600	14.377	14.4718	0.6594	10.1681	29.275
610	6.6542	6.1769	7.1729	-	-
890	12.5536	12.5935	0.3178	-	-
900	7.4835	7.7415	3.4476	4.3183	42.296
910	12.9591	12.5935	2.8212	-	-

TABLE 3. Operating cases.

Cases	Fluctuation amplitude M (°)	Fluctuation frequency ω_y (Hz)
1	9	10
2	5	10
3	9	20
4	5	20

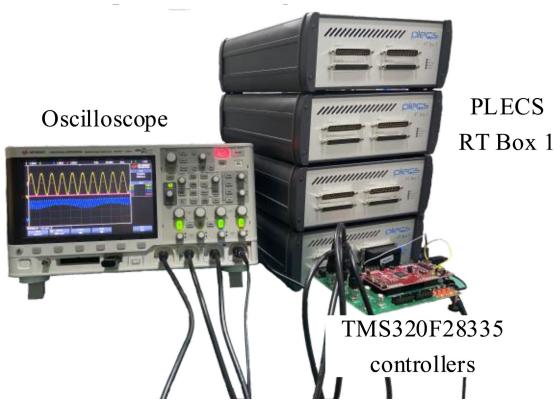

FIGURE 9. HIL platform setup.

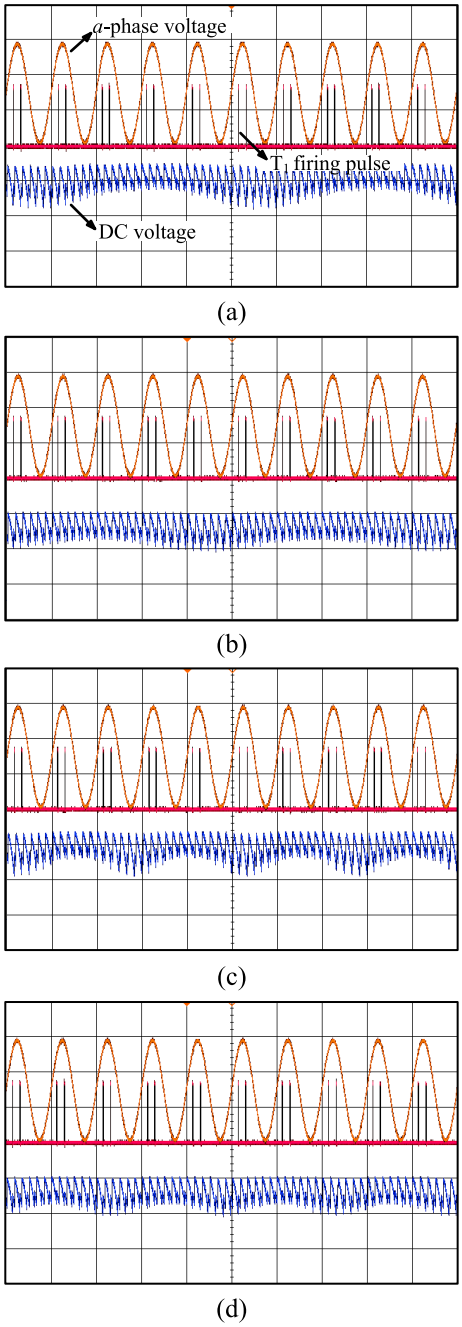

FIGURE 10. The experimental results. (a) Case 1: $M = 9°$, $\omega_Y = 10$Hz. (b) Case 2: $M = 5°$, $\omega_Y = 10$Hz. (c) Case 3: $M = 9°$, $\omega_Y = 20$Hz. (d) Case 4: $M = 5°$, $\omega_Y = 20$Hz. (*a*-phase voltage: 220 kV/div, T_1 firing pulse: 2 V/div, DC voltage: 220 kV/div, Time: 20 ms/div).

the harmonics analysis precision of the proposed method is higher than that of the traditional method since the proposed method takes the firing angle ripple and the commutation overlap angle variation into account. However, it cannot be achieved in the traditional method.

More importantly, the previous analytical methodology cannot provide results of interharmonics caused by firing angle fluctuation and overlap angle disturbance. However, the proposed approach can be applied to analyze the interharmonics based on the generation principle of firing angle in the converter. The simulation data presented in Table 2, which describe DC voltage harmonics, indicate that the relative errors of the characteristic harmonics are all reduced by at least one order of magnitude, and the relative errors of the interharmonics are almost within 3%. It verifies high-precision and availability of the proposed method again.

VI. EXPERIMENTAL TEST

The experimental tests are executed to further verify the precision of theoretical analysis based on the proposed method. The test parameters are shown in Table 1. In the experimental

tests, the digital signal processor (DSP) TMS320F28335 is used as the microcontroller, and the hardware in the loop (HIL) is used as the three-phase rectifier bridge. The setup is shown in Fig. 9.

The experimental cases are listed in Table 3. In each case, the three-phase rectifier is triggered by double-pulses. The *a*-phase voltage, T_1 firing pulse and the DC voltage are shown in Fig. 10. It is obvious that DC voltage contains

$$\begin{cases} A'_{m0} = \dfrac{1}{\pi m}\sin\dfrac{m\pi}{3}\left[J_0(mM)\cos m(\alpha_0+\dfrac{\pi}{3})+J_0(ma_1)\cos m(a_0+\dfrac{\pi}{3})\right] \\ B'_{m0} = \dfrac{1}{\pi m}\sin\dfrac{m\pi}{3}\left[J_0(mM)\sin m(\alpha_0+\dfrac{\pi}{3})+J_0(ma_1)\sin m(a_0+\dfrac{\pi}{3})\right] \\ A'_{mn} = \dfrac{1}{\pi m}\sin\dfrac{m\pi}{3}\left[J_n(mM)\cos(\dfrac{n\pi}{2}+m(\alpha_0+\dfrac{\pi}{3}))+J_n(ma_1)\cos(\dfrac{n\pi}{2}+m(a_0+\dfrac{\pi}{3}))\right] \\ B'_{mn} = \dfrac{1}{\pi m}\sin\dfrac{m\pi}{3}\left[J_n(mM)\sin(\dfrac{n\pi}{2}+m(\alpha_0+\dfrac{\pi}{3}))+J_n(ma_1)\sin(\dfrac{n\pi}{2}+m(a_0+\dfrac{\pi}{3}))\right] \end{cases} \tag{A.1}$$

$$\begin{aligned} u_{\mathrm{dc1}} = &\sum_{m=1}^{\infty}\frac{1}{2}U_{\mathrm{p}}C_{m0}J_0(mM)\left[\begin{array}{l} \cos(m+1)x\cos m\alpha_0+\sin(m+1)x\sin m\alpha_0 \\ +\cos(m-1)x\cos m\alpha_0+\sin(m-1)x\sin m\alpha_0 \\ +\cos(m+1)(x-\frac{2\pi}{3})\cos m\alpha_0+\sin(m+1)(x-\frac{2\pi}{3})\sin m\alpha_0 \\ +\cos(m-1)(x-\frac{2\pi}{3})\cos m\alpha_0+\sin(m-1)(x-\frac{2\pi}{3})\sin m\alpha_0 \\ +\cos(m+1)(x+\frac{2\pi}{3})\cos m\alpha_0+\sin(m+1)(x+\frac{2\pi}{3})\sin m\alpha_0 \\ +\cos(m-1)(x+\frac{2\pi}{3})\cos m\alpha_0+\sin(m-1)(x+\frac{2\pi}{3})\sin m\alpha_0 \end{array}\right] \\ &+\sum_{m=1}^{\infty}\frac{1}{2}U_{\mathrm{p}}C_{m0}J_0(ma_1)\left[\begin{array}{l} \cos(m+1)x\cos ma_0+\sin(m+1)x\sin ma_0 \\ +\cos(m-1)x\cos ma_0+\sin(m-1)x\sin ma_0 \\ +\cos(m+1)(x-\frac{2\pi}{3})\cos ma_0+\sin(m+1)(x-\frac{2\pi}{3})\sin ma_0 \\ +\cos(m-1)(x-\frac{2\pi}{3})\cos ma_0+\sin(m-1)(x-\frac{2\pi}{3})\sin ma_0 \\ +\cos(m+1)(x+\frac{2\pi}{3})\cos ma_0+\sin(m+1)(x+\frac{2\pi}{3})\sin ma_0 \\ +\cos(m-1)(x+\frac{2\pi}{3})\cos ma_0+\sin(m-1)(x+\frac{2\pi}{3})\sin ma_0 \end{array}\right] \end{aligned} \tag{A.2}$$

$$\begin{aligned} u_{\mathrm{dc2}} = &\sum_{m=1}^{\infty}\sum_{\substack{n=-\infty \\ n\neq 0}}^{\infty}\frac{1}{2}U_{\mathrm{p}}C_{mn}J_n(mM)\left[\begin{array}{l} \cos(m\alpha_0+\frac{n\pi}{2})\cos((m+1)x+ny)+\sin(m\alpha_0+\frac{n\pi}{2})\sin((m+1)x+ny) \\ +\cos(m\alpha_0+\frac{n\pi}{2})\cos((m-1)x+ny)+\sin(m\alpha_0+\frac{n\pi}{2})\sin((m-1)x+ny) \\ +\cos(m\alpha_0+\frac{n\pi}{2})\cos((m+1)(x-\frac{2\pi}{3})+ny)+\sin(m\alpha_0+\frac{n\pi}{2})\sin((m+1)(x-\frac{2\pi}{3})+ny) \\ +\cos(m\alpha_0+\frac{n\pi}{2})\cos((m-1)(x-\frac{2\pi}{3})+ny)+\sin(m\alpha_0+\frac{n\pi}{2})\sin((m-1)(x-\frac{2\pi}{3})+ny) \\ +\cos(m\alpha_0+\frac{n\pi}{2})\cos((m+1)(x+\frac{2\pi}{3})+ny)+\sin(m\alpha_0+\frac{n\pi}{2})\sin((m+1)(x+\frac{2\pi}{3})+ny) \\ +\cos(m\alpha_0+\frac{n\pi}{2})\cos((m-1)(x+\frac{2\pi}{3})+ny)+\sin(m\alpha_0+\frac{n\pi}{2})\sin((m-1)(x+\frac{2\pi}{3})+ny) \end{array}\right] \\ &+\sum_{m=1}^{\infty}\sum_{\substack{n=-\infty \\ n\neq 0}}^{\infty}\frac{1}{2}U_{\mathrm{p}}C_{mn}J_n(ma_1)\left[\begin{array}{l} \cos(ma_0+\frac{n\pi}{2})\cos((m+1)x+ny)+\sin(ma_0+\frac{n\pi}{2})\sin((m+1)x+ny) \\ +\cos(ma_0+\frac{n\pi}{2})\cos((m-1)x+ny)+\sin(ma_0+\frac{n\pi}{2})\sin((m-1)x+ny) \\ +\cos(ma_0+\frac{n\pi}{2})\cos((m+1)(x-\frac{2\pi}{3})+ny)+\sin(ma_0+\frac{n\pi}{2})\sin((m+1)(x-\frac{2\pi}{3})+ny) \\ +\cos(ma_0+\frac{n\pi}{2})\cos((m-1)(x-\frac{2\pi}{3})+ny)+\sin(ma_0+\frac{n\pi}{2})\sin((m-1)(x-\frac{2\pi}{3})+ny) \\ +\cos(ma_0+\frac{n\pi}{2})\cos((m+1)(x+\frac{2\pi}{3})+ny)+\sin(ma_0+\frac{n\pi}{2})\sin((m+1)(x+\frac{2\pi}{3})+ny) \\ +\cos(ma_0+\frac{n\pi}{2})\cos((m-1)(x+\frac{2\pi}{3})+ny)+\sin(ma_0+\frac{n\pi}{2})\sin((m-1)(x+\frac{2\pi}{3})+ny) \end{array}\right] \end{aligned} \tag{A.3}$$

TABLE 4. DC Voltage harmonic comparison between experiment and proposed method.

Frequency(Hz)	Experiment (kV)	Proposed method(kV)	Error (%)
0	446.9447	448.5853	0.3671
10	25.7980	24.84	3.7134
290	15.2882	13.7855	9.8291
300	59.9321	58.2725	2.7691
310	13.4866	13.7855	2.2163
590	5.8645	6.1769	5.3269
600	14.5369	14.4718	0.4478
610	6.7635	6.1769	8.6730
890	12.5853	12.5935	0.0652
900	7.8146	7.7415	0.9354
910	12.6680	12.5935	0.5881

fluctuation with the same frequency as the firing angle and the subsequent overlap angle.

To further verify the effectiveness of the proposed harmonic analysis method, the experimental data of DC voltage harmonics in case 1 is presented in Table. 4.

VII. CONCLUSION

In this paper, an accurate harmonics analysis method for LCC is proposed under the condition of firing angle fluctuation. The transmission mechanism of interharmonics caused by the firing angle ripple and the subsequent commutation overlap angle variation is elaborated. The accuracy and correctness of the proposed method are verified by the simulation in PSCAD/EMTDC and experimental test. The main contributions and conclusions are summarized as follow:

1) The analysis for harmonic transmission of LCC in the proposed method takes the firing angle fluctuation and the subsequent overlap angle fluctuation into account. The max fitting error is less than 0.5°.
2) The proposed method can be applied to calculate both characteristic and interharmonics of DC voltage, and the interharmonics are not considered in the previous method. Furthermore, the relative errors of the interharmonics are almost within 3%.
3) For characteristic harmonics, the analysis accuracy of the proposed method is still higher than that of the traditional method, and the relative errors can be reduced by at least one order of magnitude.

Moreover, the proposed method can be easily extended to asymmetrical modulation and unbalanced conditions in LCC.

APPENDIX

The coefficients for (15) are expressed in detailed by (A.1), as shown at the bottom of the previous page. Meanwhile, u_{dc1} and u_{dc2} with commutation overlap angle variation can be expressed in detailed by (A.2), (A.3), as shown at the bottom of the previous page, respectively.

REFERENCES

[1] Z. Zhang, Z. Xu, Y. Xue, and G. Tang, "DC-side harmonic currents calculation and DC-loop resonance analysis for an LCC–MMC hybrid HVDC transmission system," *IEEE Trans. Power Del.*, vol. 30, no. 2, pp. 642–651, Apr. 2015.
[2] K. Sun, H. Xiao, J. Pan, and Y. Liu, "A station-hybrid HVDC system structure and control strategies for cross-seam power transmission," *IEEE Trans. Power Syst.*, early access, Jun. 15, 2020, doi: 10.1109/TPWRS.2020.3002430.
[3] E. Kontos, G. Tsolaridis, R. Teodorescu, and P. Bauer, "High order voltage and current harmonic mitigation using the modular multilevel converter STATCOM," *IEEE Access*, vol. 5, pp. 16684–16692, 2017.
[4] K. Sun, H. Xiao, S. Liu, and Y. Liu, "A machine learning-based fast frequency response control for a VSC-HVDC system," *CSEE J. Power Energy Syst.*, early access, Oct. 6, 2020, doi: 10.17775/CSEEJPES.2020.01410.
[5] K. Sun, K.-J. Li, W.-J. Lee, Z.-D. Wang, W. Bao, Z. Liu, and M. Wang, "VSC-MTDC system integrating offshore wind farms based optimal distribution method for financial improvement on wind producers," *IEEE Trans. Ind. Appl.*, vol. 55, no. 3, pp. 2232–2240, May 2019, doi: 10.1109/TIA.2019.2897672.
[6] S. Yang, Z. Shao, W. Zheng, and F. Chen, "Mitigation of background harmonics effect on MMC controller based on a novel coordinate transformation technique," *IEEE Access*, vol. 7, pp. 167113–167126, 2019.
[7] R. Wang, Q. Sun, D. Ma, and Z. Liu, "The small-signal stability analysis of the droop-controlled converter in electromagnetic timescale," *IEEE Trans. Sustain. Energy*, vol. 10, no. 3, pp. 1459–1469, Jul. 2019.
[8] R. Wang, Q. Sun, D. Ma, D. Qin, Y. Gui, and P. Wang, "Line inductance stability operation domain assessment for weak grids with multiple constant power loads," *IEEE Trans. Energy Convers.*, early access, Sep. 2, 2020, doi: 10.1109/TEC.2020.3021070.
[9] L. Hu and R. Yacamini, "Harmonic transfer through converters and HVDC links," *IEEE Trans. Power Electron.*, vol. 7, no. 3, pp. 514–525, Jul. 1992.
[10] L. Hu and R. E. Morrison, "The use of modulation theory to calculate the harmonic distortion in HVDC systems operating on an unbalanced supply," *IEEE Trans. Power Syst.*, vol. 12, no. 2, pp. 973–980, May 1997.
[11] K. Sadek and M. Pereira, "Harmonic transfer in HVDC systems under unbalanced conditions," *IEEE Trans. Power Syst.*, vol. 14, no. 4, pp. 1394–1399, Nov. 1999.
[12] S. Liu, X. Cui, Z. Z. Lin, Z. Lian, Z. Lin, F. Wen, Y. Ding, Q. Wang, L. Yang, R. Jin, and H. Qiu, "Practical method for mitigating three-phase unbalance based on data-driven user phase identification," *IEEE Trans. Power Syst*, vol. 2, no. 35, pp. 1653–1657, Mar. 2020.
[13] Y. Jiang and A. Ekstrom, "General analysis of harmonic transfer through converters," *IEEE Trans. Power Electron.*, vol. 12, no. 2, pp. 287–293, Mar. 1997.
[14] K. L. Lian, B. K. Perkins, and P. W. Lehn, "Harmonic analysis of a three-phase diode bridge rectifier based on sampled-data model," *IEEE Trans. Power Del.*, vol. 23, no. 2, pp. 1088–1096, Apr. 2008.
[15] A. R. Wood and J. Arrillaga, "HVDC convertor waveform distortion: A frequency-domain analysis," *Proc. IEE-Gener. Transmiss. Distrib.*, vol. 142, no. 1, pp. 88–96, Jan. 1995.
[16] R. Carbone, F. DeRosa, R. Langella, and A. Testa, "A new approach for the computation of harmonics and interharmonics produced by line-commutated AC/DC/AC converters," *IEEE Trans. Power Del.*, vol. 20, no. 3, pp. 2227–2234, Jul. 2005.
[17] J. B. Kwon, X. Wang, F. Blaabjerg, C. L. Bak, A. R. Wood, and N. R. Watson, "Harmonic instability analysis of a single-phase grid-connected converter using a harmonic state-space modeling method," *IEEE Trans. Ind. Appl.*, vol. 52, no. 5, pp. 4188–4200, Sep. 2016.
[18] J. Kwon, X. Wang, F. Blaabjerg, C. L. Bak, V.-S. Sularea, and C. Busca, "Harmonic interaction analysis in a grid-connected converter using harmonic state-space (HSS) modeling," *IEEE Trans. Power Electron.*, vol. 32, no. 9, pp. 6823–6835, Sep. 2017.
[19] J. Lyu, X. Zhang, X. Cai, and M. Molinas, "Harmonic state-space based small-signal impedance modeling of a modular multilevel converter with consideration of internal harmonic dynamics," *IEEE Trans. Power Electron.*, vol. 34, no. 3, pp. 2134–2148, Mar. 2019.
[20] Y. Zhang and Y. W. Li, "Investigation and suppression of harmonics interaction in high-power PWM current-source motor drives," *IEEE Trans. Power Electron.*, vol. 30, no. 2, pp. 668–679, Feb. 2015.
[21] X. Li, Y. Wang, and W. Xu, "A new filtering scheme for HVDC terminals based on damped high-pass filter," *IEEE Trans. Power Del.*, vol. 34, no. 5, pp. 2050–2057, Oct. 2019.

[22] Y. Xue, X.-P. Zhang, and C. Yang, "AC filterless flexible LCC HVDC with reduced voltage rating of controllable capacitors," *IEEE Trans. Power Syst.*, vol. 33, no. 5, pp. 5507–5518, Sep. 2018.
[23] A. Testa, M. F. Akram, and R. Burch, "Interharmonics: Theory and modeling," *IEEE Trans. Power Del.*, vol. 22, no. 4, pp. 2335–2348, Oct. 2007.
[24] J. Hui, W. Xu, and H. Yang, "A method to determine the existence of genuine interharmonics," *IEEE Trans. Power Del.*, vol. 27, no. 3, pp. 1690–1692, Jul. 2012.
[25] H. Soltani, P. Davari, F. Zare, P. C. Loh, and F. Blaabjerg, "Characterization of input current interharmonics in adjustable speed drives," *IEEE Trans. Power Electron.*, vol. 32, no. 11, pp. 8632–8643, Nov. 2017.
[26] H. Soltani, P. Davari, F. Zare, and F. Blaabjerg, "Effects of modulation techniques on the input current interharmonics of adjustable speed drives," *IEEE Trans. Ind. Electron.*, vol. 65, no. 1, pp. 167–178, Jan. 2018.
[27] S. Mirsaeidi, X. Dong, D. Tzelepis, D. M. Said, A. Dysko, and C. Booth, "A predictive control strategy for mitigation of commutation failure in LCC-based HVDC systems," *IEEE Trans. Power Electron.*, vol. 34, no. 1, pp. 160–172, Jan. 2019.

HE HUANG was born in Hubei, China, in 1995. He received the B.S. degree in electrical engineering from Sichuan University, Chengdu, China, in 2018, where he is currently pursuing the master's degree with the College of Electrical Engineering. His current research interests include harmonic analysis and high-voltage direct current.

Mr. Huang was a recipient of the Best Paper Award from the IEEE International Electrical and Energy Conference (CIEEC).

JUNPENG MA (Member, IEEE) received the B.S. and Ph.D. degrees in electrical engineering from Southwest Jiaotong University, Chengdu, China, in 2013 and 2018, respectively.

He was a Guest Ph.D. Student with Aalborg University, from November 2017 to May 2018. He is currently an Associate Research Fellow with the College of Electrical Engineering, Sichuan University, Chengdu. His research topics include the modeling and control of grid-connected multilevel converters applied in the traction drive system, the new energy field, and the HVDC systems.

Dr. Ma was a recipient of the Best Paper Award from the IEEE International Electrical and Energy Conference (CIEEC).

SHUNLIANG WANG (Member, IEEE) received the B.S. and Ph.D. degrees in electrical engineering from Southwest Jiaotong University, Chengdu, China, in 2010 and 2016, respectively.

From 2017 to 2018, he was a Visiting Scholar with the Department of Energy Technology, Aalborg University, Denmark. He is currently an Associate Professor with the College of Electrical Engineering, Sichuan University. His current research interests include control, modulation, and modeling of power converters in high voltage direct current, renewable energy field, and railway traction systems.

Dr. Wang was a recipient of the Best Paper Award at the IEEE International Electrical and Energy Conference (CIEEC) in 2019.

YUQING DONG was born in Jiangsu, China, in 1995. She received the B.S. degree from Sichuan University, Chengdu, China, in 2017, where she is currently pursuing the Ph.D. degree with the College of Electrical Engineering and Information Technology. Her current research interests include high voltage direct current and harmonic instability.

NING JIAO (Student Member, IEEE) was born in Hebei, China, in 1994. She received the B.S. degree from Sichuan University, Chengdu, China, in 2018, where she is currently pursuing the master's degree with the College of Electrical Engineering and Information Technology. Her current research interests include modulation of power converters and high voltage direct current.

TIANQI LIU (Senior Member, IEEE) received the B.S. and M.S. degrees from Sichuan University, Chengdu, China, in 1982 and 1986, respectively, and the Ph.D. degree from Chongqing University, Chongqing, China, in 1996, all in electrical engineering.

She is currently a Professor with the College of Electrical Engineering, Sichuan University. Her research interests include power system analysis and stability control, HVDC, optimal operation, dynamic security analysis, dynamic state estimation, and the load forecast.